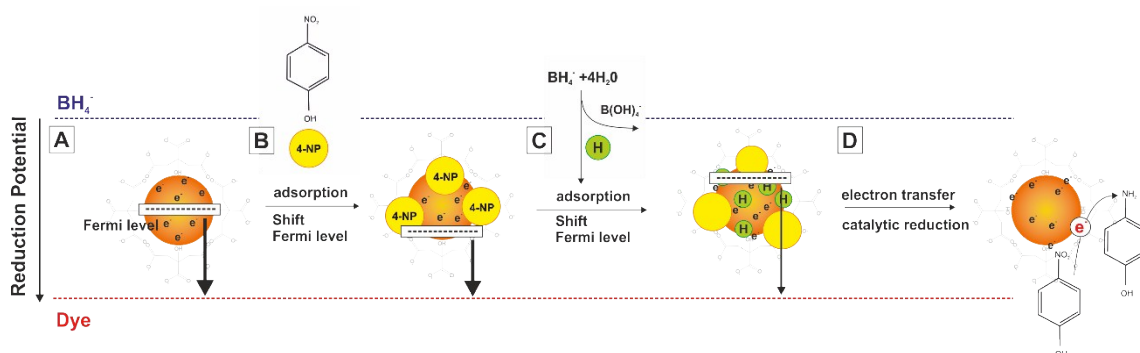


## Electronic Supplementary Information

### Probing the Surface Reactivity of Nanocrystals by the Catalytic Degradation of Organic Dyes: The Effect of Size, Surface Chemistry and Composition.

Jordi Piella, Florind Merkoçi, Aziz Genç, Jordi Arbiol, Neus G. Bastús and Victor Puntes



**Figure S1.** Electro-chemical mechanism of catalytic reduction of dyes by metal NCs in the presence of  $\text{BH}_4^-$  and changes of the Fermi level of metal NCs during the process.

The Fermi potential of the metal NCs can be shifted to positive or to negative potentials by the adsorption of electrophile (dyes) or nucleophile species ( $\text{BH}_4^-$  ions) respectively. **Figure S1B-C** schematically illustrates the changes of the Fermi level of metal NCs during the catalytic process. Thus, after the adsorption of dyes molecules, the Fermi potential of the metal NCs shift to relatively high values (Fig. S1-B). However, after the addition and further adsorption of  $\text{BH}_4^-$  ions the Fermi level of the metal NCs decreases (Fig. S1-C) promoting the transfer of electrons from the nucleophile to the dye via the metal NC, driving its reduction to the corresponding reduced forms (Fig. S1-D).

The particular mechanism of the catalytic reduction of the various dyes used in this work can be explained as follows.

**Degradation of 4-nitrophenol to 4-aminophenol.** The catalytic reduction of 4-NP into 4-aminophenol (4-AP) by  $\text{NaBH}_4$  is an electrochemical process in which the metal NCs have the main role of acting as electron relay systems, transferring the electrons from the donor ( $\text{BH}_4^-$ ) to the acceptor (4-NP). In detail, in the reaction aqueous solution,  $\text{BH}_4^-$  ions are adsorbed on and react with the surface of metal NCs, thereby creating active metal hydrides at their surface. At the same time, 4-NP also adsorbs on the surface of metal NCs. These two steps are reversible and are fitted into a Langmuir isotherm model. The diffusion of both reactants to the surface of metal NCs and the adsorption/desorption equilibriums of these reactants on the surface is also fast. Therefore, the reduction of 4-NP to corresponding 4-AP occurs in view of the reaction of adsorbed 4-NP with the metal hydrides bound by metal NC surface. A first mechanistic insight was provided by Fritz Haber in the late 1890s using electrochemical methods.<sup>1</sup> From Haber's mechanistic scheme, there are two main paths to get the final products: the direct path and the condensation path. The

direct route is a stepwise hydrogenation process involving the formation of two intermediate products, nitrosobenzene and phenylhydroxylamine. In the condensation route, intermediate product was azobenzene.<sup>2</sup> When formed, 4-AP detaches from the metal NCs surface, the next cycle of new catalytic reduction can be triggered again.

**Degradation of MB to Leuco MB and RhB to Leuco RhB.** The catalytic reduction of RhB and MB can be also explained by an electrochemical mechanism, where the metal NCs serve as an electron relay system for the oxidant and reductant species. First  $\text{BH}_4^-$  ions and MB or RhB molecules are adsorbed together onto the surface of the metal NCs. Then electron transfer takes place between the dyes and  $\text{BH}_4^-$  through particle surface. After receiving the electrons, the dye molecules are reduced to Leuco MB or Leuco RhB.<sup>3</sup>

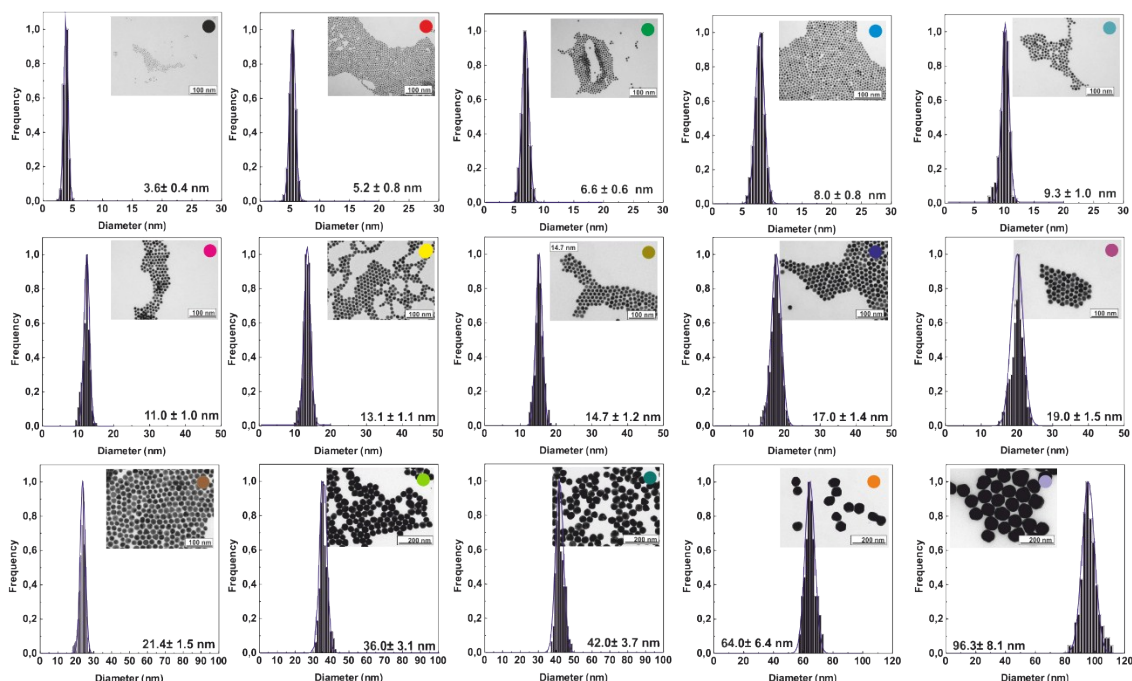


**Figure S2.** TEM images analysis of Au NPs shown in Figure 1. Au seeds diameter increase from ~3.6 to ~110 nm after different growth steps. At least 1000 NPs were counted for each size.

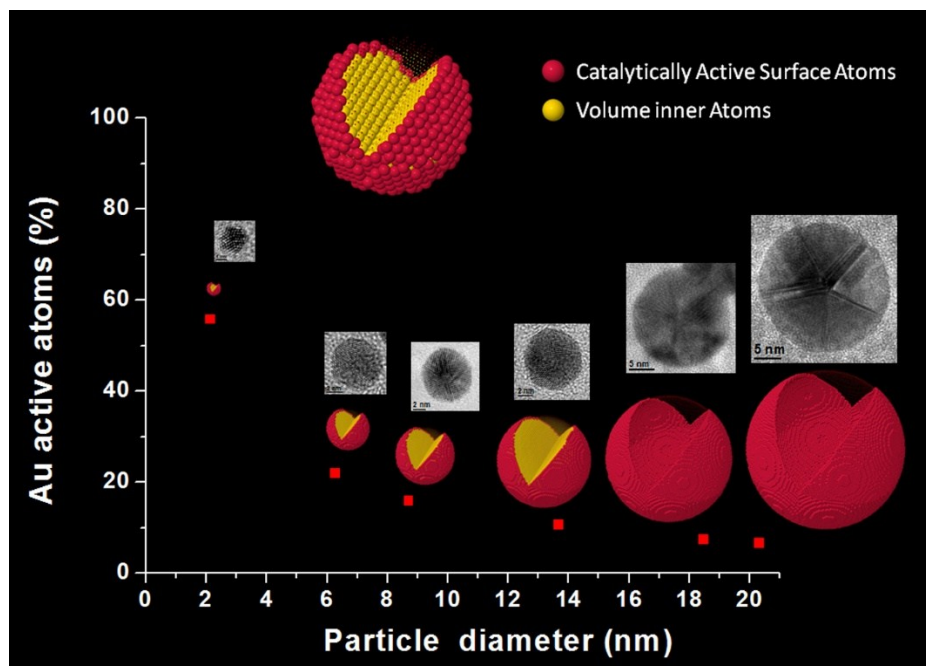


**Figure S3.** Comparison of the ratio of catalytically active Au atoms for 2, 5, 10, 15, 20 and 30 nm NCs. The ratio of Au active atoms if found to be 55.83%, 21.97%, 15.95%, 10.63%, 7.48% and 6.67%, respectively. Corresponding HRTEM experimental images for all the simulated models are also presented.

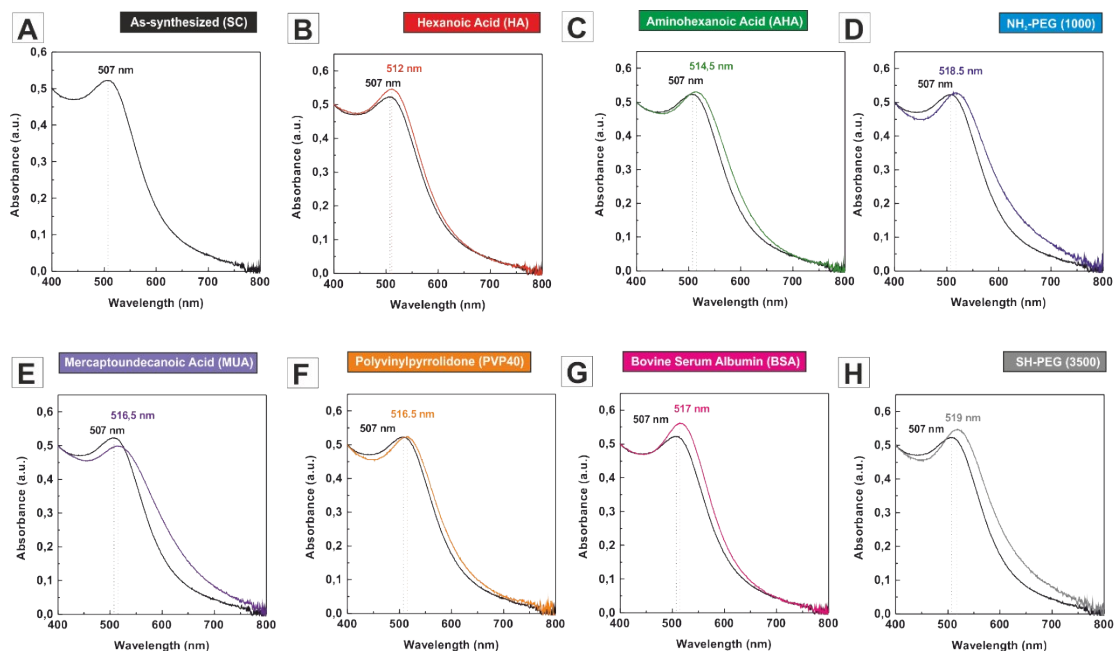


**Figure S4. Surface coating of Au NPs.** UV-Vis spectroscopy of as-synthesized (A), hexanoic acid (B), amino hexanoic acid (C), NH<sub>2</sub>-PEG (1000) (D), mercaptoundecanoic acid (E), polyvinylpyrrolidone (F), and bovine serum albumin (BSA) (G) and SH-PEG (3500) (H).

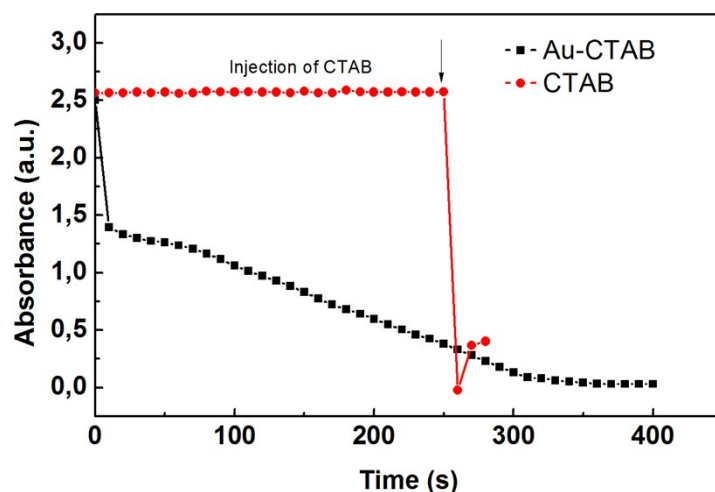


**Figure S5.** CTAB degradation of 4-Nitrophenol. The catalytic performance of CTAB was evaluated by added an aqueous solution of CTAB molecules (0.1 mL, 10 mM) into a solution of 4-NP and NaBH<sub>4</sub>, obtaining that CTAB molecules are able to rapidly degrade 4-NP by themselves. Similarly, the drop observed at short reaction times for CTAB-coated Au NCs can be attributed to the free of bound CTAB molecules.

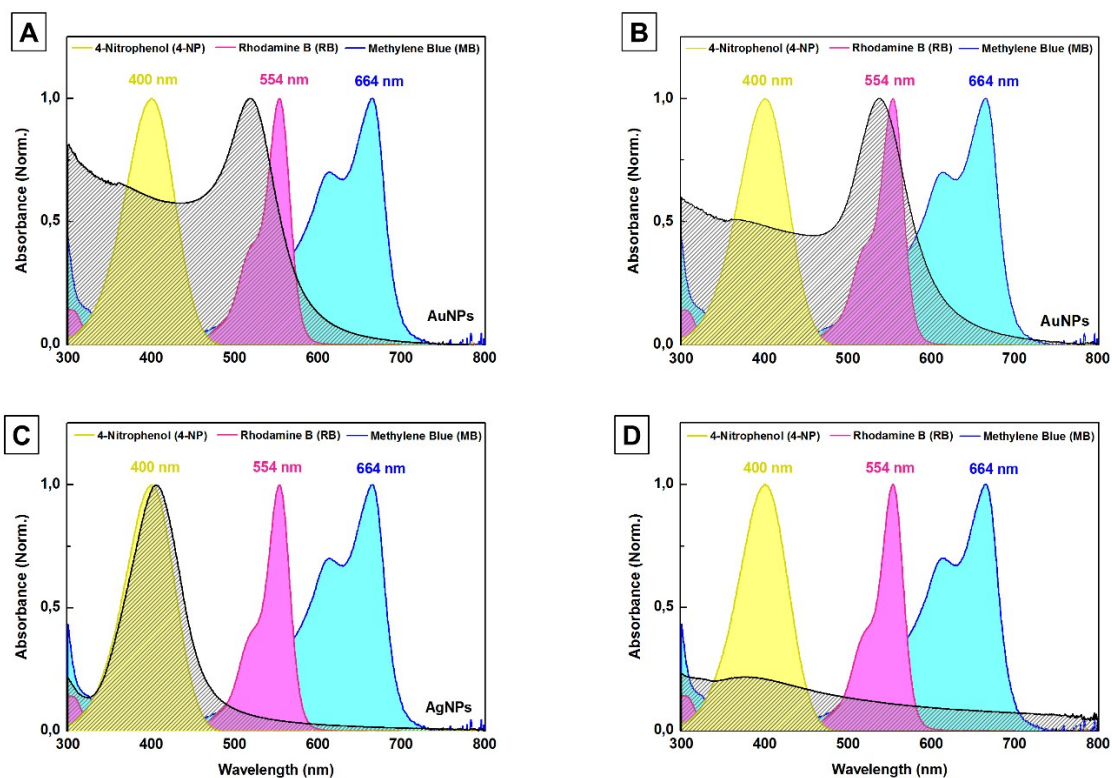


**Figure S6.** Optical interference between 4-Nitrophenol, Rhodamine B and Methylene blue and Au NCs of 10 nm (A), 50 nm (B), Ag NCs (C) and Pt NCs (D). In the case of Au and Ag spectra were normalized to the maximum absorption of the dyes.

## Au NP Modelling and Simulation Studies

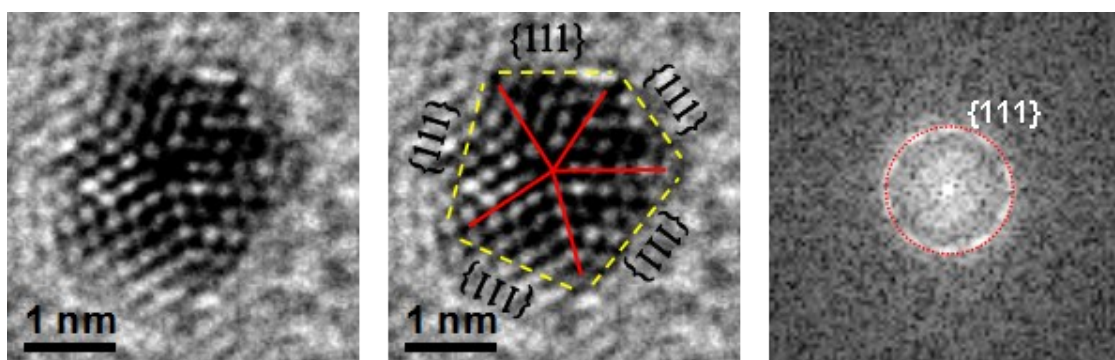


**Figure S7.** HRTEM image of a 2.6 nm decahedron shaped nanoparticle and corresponding power spectrum (FFT) image of the nanoparticle.

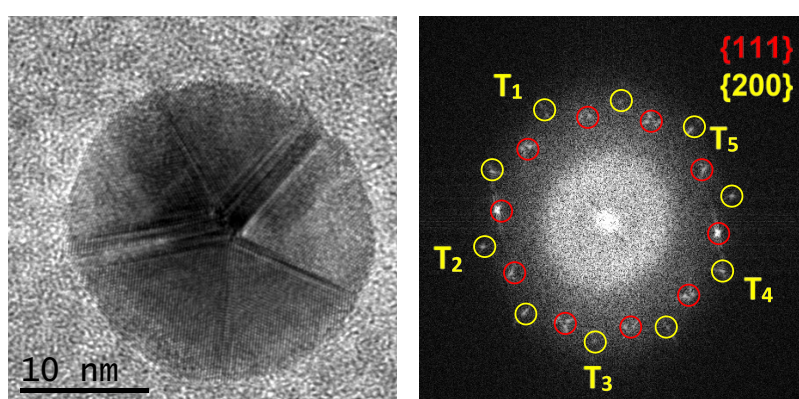


**Figure S8.** HRTEM image and corresponding power spectrum (FFT) of a 24.4 nm nanoparticle. Diffraction spots corresponding to  $\{111\}$  and  $\{200\}$  family of planes form a perfect symmetry, which is typical for this kind of decahedrons.<sup>4-6</sup>

On the basis of above presented HRTEM observations, we propose a model of spheroidal decahedron shape particles, which is present in all samples. We must say here, that for bigger nanoparticles the  $\{111\}$  external facets tend to be sharper and the nanoparticles have a morphology closer to the ideal decahedron, losing the spheroidal shape. Regular decahedron shape consists of the merging of 5  $\{111\}$  faceted tetrahedral.<sup>5, 7, 8</sup> Yet, the theoretical angle between to (111) planes is  $70.53^\circ$  and combination of 5 tetrahedrons to form a decahedron results in a  $7.35^\circ$  gap<sup>7</sup>, which must be filled by some form of internal strain such as dislocations and other structural defects.<sup>6, 8</sup> Johnson et al.<sup>8</sup> reports that elastic anisotropy, results in an internal lattice rotation of  $4.3^\circ$ , combined with about  $0.6^\circ$  shear-strain for each tetrahedron accommodate this  $7.35^\circ$  gap in their experimental decahedron shaped Au nanoparticle.

Here, we assume a homogeneous distribution of these strains to form a regular decahedron out of 5  $\{111\}$  faceted tetrahedra with a rotation angle of  $72^\circ$ .

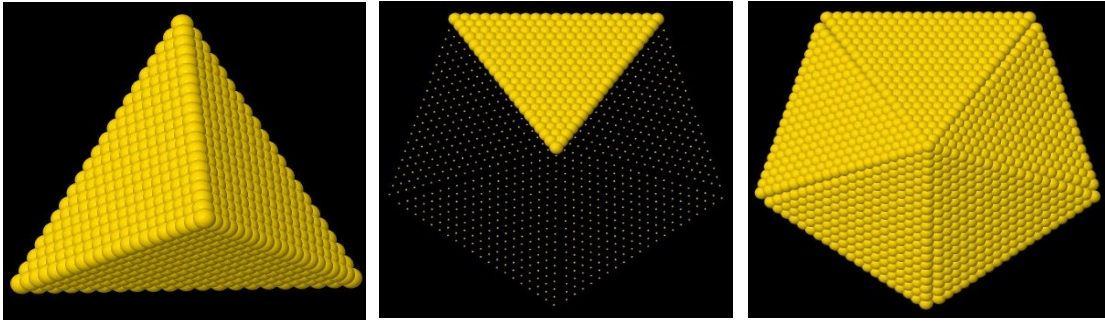


**Figure S9.** Modeling a regular Au decahedron with a size of 10 nm: (i) creation of a  $\{111\}$  faceted tetrahedron, (ii)-(iii) combination of 5 individual tetrahedra with sequential rotations of  $72^\circ$ .

In Figure S9 we have modeled a regular Au decahedron with a size of 10 nm. Figure S6 shows the stages of this modeling process. However, as can be seen in the above presented HRTEM images, such a model cannot be representative for the present samples. Most of the reported Au decahedral shapes having sizes smaller than 30 nm reveals similar spheroidal behavior<sup>5-7</sup>, however, modeling and simulation studies are conducted as if they were perfect decahedrons.<sup>7,9</sup>

Due to above presented discrepancy between experimentally observed nanoparticles and suggested regular decahedral models, we propose a spheroidal decahedron model, which contains 5  $\{111\}$  facets but has a spheroidal like structure.

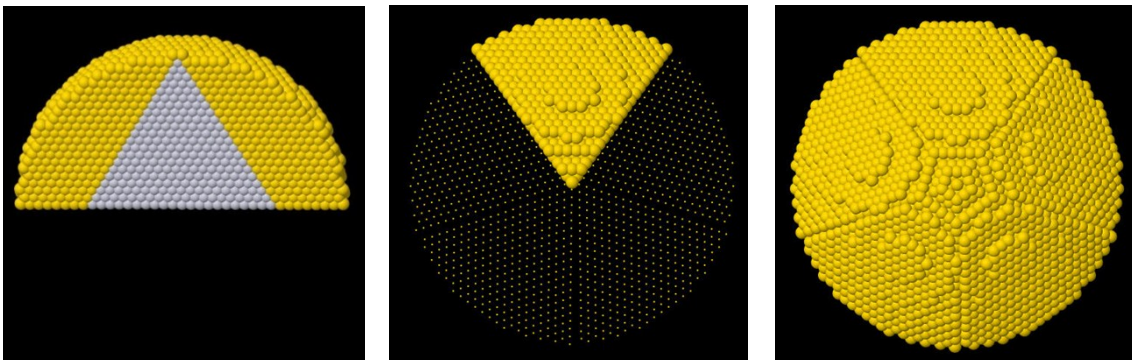


**Figure S10.** Modeling a spheroidal Au decahedron with a diameter of 10 nm: (i) creation of a  $\{111\}$  faceted spheroidal subunit, (ii)-(iii) combination of 5 individual subunits with sequential rotations of  $72^\circ$ .

Figure S10 shows the steps of the spheroidal decahedron modeling process. First, we have created a  $\{111\}$  faceted segment over a tetrahedron. Then, we merge 5 of them with a sequential rotations of  $72^\circ$  forming a 5 twinned spheroidal decahedral structure.

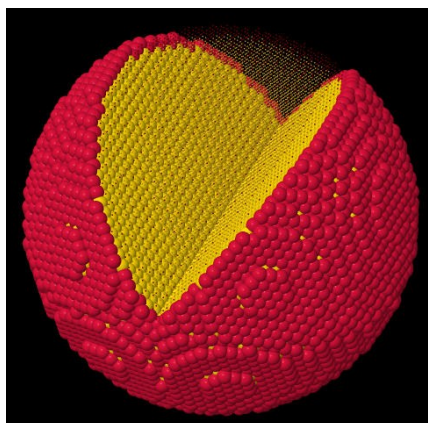


**Figure S11.** A spheroidal Au decahedron with a diameter of 10 nm, showing the surface active atoms in red.

We extended the spheroidal decahedral model and added a shell in order to calculate the ratio of catalytically active surface atoms over volume atoms. Figure S11 shows the catalytically active surface atoms in red and volume atoms in yellow. For the case of 10 nm spheroidal decahedron, total number of atoms is found to be 30245, where 4272 of the total atoms are in the surface. Percent ratio of catalytically active surface Au atoms is 14.12% for this model.

In addition to 10 nm model, we have modeled particles with different sizes such as 1 nm, 2 nm, 4 nm, 6 nm, 8 nm, 12 nm and 15 nm in order to compare the variation of the ratio of surface active Au atoms with size (**Fig. S12**).

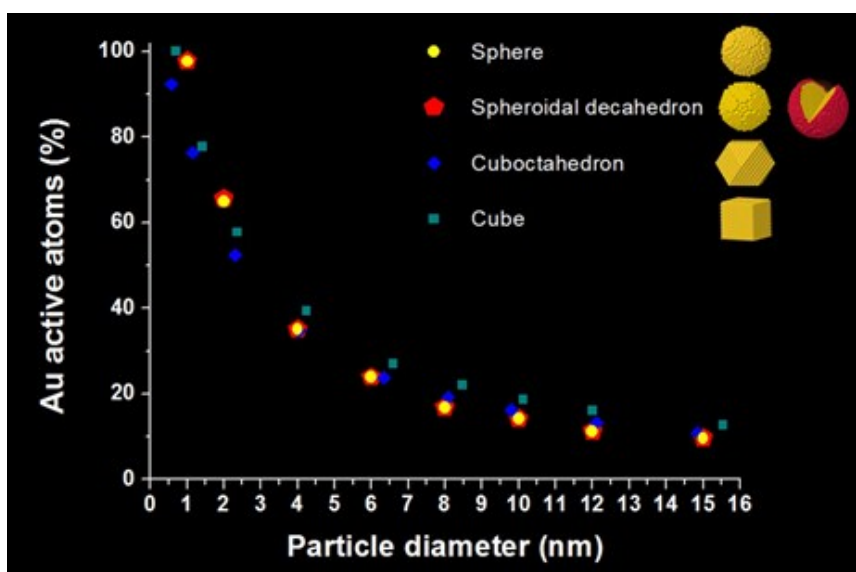


**Figure S12.** Comparison of the ratio of catalytically active Au atoms with increasing particle diameters for different Au nanostructures such as sphere, spheroidal decahedron, cuboctahedron and cube. The results plotted here have been summarized in an animated video movie that can be reached by following the link in ref <sup>10</sup>.

1. F. Haber, *Z. Elektrochem. Angew. Phys. Chem*, 1898, 506-514.
2. Z. Li, X. Xu, X. Jiang, Y. Li, Z. Yu and X. Zhang, *RSC Adv.*, 2015, **5**, 30062-30066.
3. B. R. Ganapuram, M. Alle, R. Dadigala, A. Dasari, V. Maragoni and V. Guttena, *International Nano Letters*, 2015, **5**, 215-222.
4. H. Hofmeister, *Mater. Sci. Forum*, 1999, **312**, 325-332.
5. L.-F. Zhang, L. Wang, S.-L. Zhong, Y.-X. Huang and A.-W. Xu, *Dalton Transactions*, 2012, **41**, 4948-4954.
6. J. L. Elechiguerra, J. Reyes-Gasga and M. J. Yacaman, *J. Mater. Chem.*, 2006, **16**, 3906-3919.
7. C. Y. Yang, *J. Cryst. Growth*, 1979, **47**, 274-282.
8. C. L. Johnson, E. Snoeck, M. Ezcurdia, B. Rodriguez-Gonzalez, I. Pastoriza-Santos, L. M. Liz-Marzan and M. J. Hytch, *Nat Mater*, 2008, **7**, 120-124.
9. Z. W. Wang and R. E. Palmer, *Phys. Rev. Lett.*, 2012, **108**, 245502.
10. <http://gaen.cat/research/295>